Exploring Reaction Pathways for *O*-GlcNAc Transferase Catalysis. A String Method Study

Manju Kumari,[†,‡,∥] Stanislav Kozmon,[†,‡,◆,∥] Petr Kulhánek,[†,‡] Jakub Štepán,[‡] Igor Tvaroška,[†,§] and Jaroslav Koča*[,†,‡]

†Central European Institute of Technology (CEITEC), Masaryk University, Kamenice 5, 625 00 Brno, Czech Republic
‡Faculty of Science - National Centre for Biomolecular Research, Masaryk University, Kamenice 5, 625 00 Brno, Czech Republic
§Institute of Chemistry, Slovak Academy of Sciences, Dúbravská cesta 9, 845 38 Bratislava, Slovak Republic

Ⓢ Supporting Information

ABSTRACT: The inverting *O*-GlcNAc glycosyltransferase (OGT) is an important post-translation enzyme, which catalyzes the transfer of *N*-acetylglucosamine from UDP-*N*-acetylglucosamine (UDP-GlcNAc) to the hydroxyl group of the Ser/Thr of cytoplasmic, nuclear, and mitochondrial proteins. In the past, three different catalytic bases were proposed for the reaction: His498, α-phosphate, and Asp554. In this study, we used hybrid quantum mechanics/molecular mechanics (QM/MM) Car−Parrinello molecular dynamics to investigate reaction paths using α-phosphate and Asp554 as the catalytic bases. The string method was used to calculate the free-energy reaction profiles of the tested mechanisms. During the investigations, an additional mechanism was observed. In this mechanism, a proton is transferred to α-phosphate via a water molecule. Our calculations show that the mechanism with α-phosphate acting as the base is favorable. This reaction has a rate-limiting free-energy barrier of 23.5 kcal/mol, whereas reactions utilizing Asp554 and water-assisted α-phosphate have barriers of 41.7 and 40.9 kcal/mol, respectively. Our simulations provide a new insight into the catalysis of OGT and may thus guide rational drug design of transition-state analogue inhibitors with potential therapeutic use.
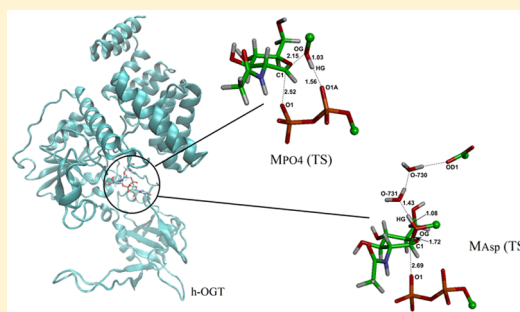
1. INTRODUCTION

A vast repertoire of glycan structures present inside the cell requires a variety of glycosyltransferases and glycoside hydrolases working synergistically through the formation and breakage of glycosidic linkages, respectively, to maintain a balance between the various glycans and glycoconjugates. These glycoconjugates are a collection of glycoproteins, proteoglycans, and glycolipids and are formed by the sequential action of glycosyltransferases, augmenting the structural and functional diversity of proteins. Glycosyltransferases (GTs) transfer sugar moieties onto various acceptors such as proteins, lipids, oligosaccharides, and natural products.[1−3] *O*-GlcNAc transferase (OGT) is an important enzyme in the family of *O*-glycosyltransferases, catalyzing the transfer of *N*-acetylglucosamine from UDP-*N*-acetylglucosamine (UDP-GlcNAc) to the hydroxyl group of Ser/Thr of cytoplasmic, nuclear, and mitochondrial proteins.[4] Such GlcNAc glycosylated proteins include numerous transcription factors, tumor suppressors, kinases, phosphatases, and histone-modifying proteins.[5,6] Knocking down the corresponding OGT gene was found to be lethal in mice, reflecting the critical importance of *O*-GlcNAc glycosylation for cell survival.[7,8] Aberrant glycosylation by OGT has also been linked to diabetic complications, cancer, and neurodegenerative diseases including Alzheimer's disease.[5,9−11] The critical importance of OGT to cell vitality has drawn

attention to investigating the catalysis process, but, unfortunately, the mechanism of the catalysis is still unclear. Understanding the reaction mechanism at the atomic level and determining the transition state will provide a rational basis for designing transition-state−analogue-based drugs/inhibitors, which can be potential therapeutic contenders for the treatment of diseases whose origin is from an impaired functioning of OGT and/or misregulation of *O*-glycosylation pathways.[12]

Human OGT (h-OGT) is a member of the GT-B superfamily, and currently its crystal structures are available with/without donor/acceptor in the PDB database.[13−15] The X-ray crystal structures available have a variation in their donor UDG (UDP-GlcNAc) and acceptor (CKII peptide) substrates. The key residues in the catalytic site of OGT are the His498, His558, Gln839, Lys842, Lys898, His901, and His920 amino acids.[13] These residues either actively participate in catalysis or passively stabilize the system during the reaction. The Ser21 from the peptide CKII acts as an acceptor for GlcNAc. Oriented water molecules were also observed at the catalytic site.
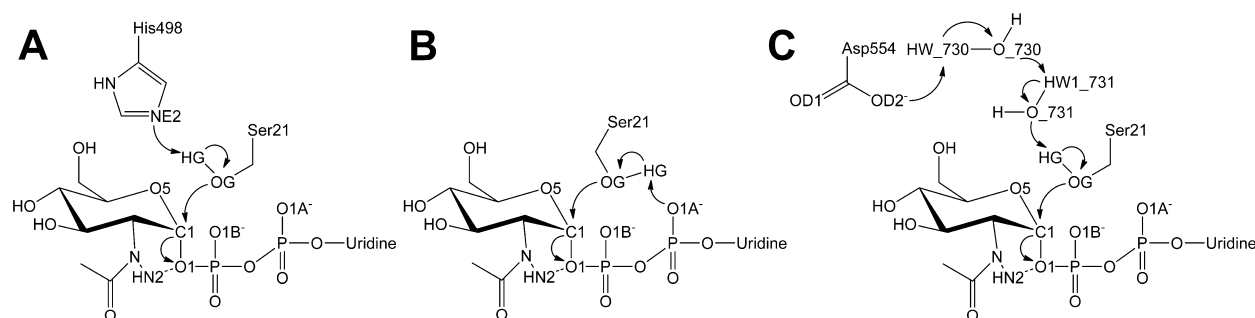
Figure 1. Schematic representation of the proposed mechanisms: (A) His498 ($\mathbf{M_{His}}$) as a catalytic base;[13] (B) α-phosphate ($\mathbf{M_{PO4}}$) as a catalytic base;[14] (C) the proton from Ser21 indirectly moves to Asp554 via the Grotthuss mechanism supported by two bridging water molecules ($\mathbf{M_{Asp}}$).[15] Curved arrows represent the movement of an electron. Selected atom names correspond to the PDB nomenclature.

The structures published in 2011 and 2012, supported by experimental biochemical data, suggested three possible mechanisms. Lazarus and Walker published the first h-OGT structure, and their biochemical analysis data of H498A mutant showed a decrease in OGT catalytic activity, suggesting the involvement of the His498 residue as the catalytic base (Figure 1A).[13] This mechanism was further explored through theoretical calculations at the DFT QM/MM level of theory in our previous work.[16] Calculations of adiabatic energy surfaces showed that a proposed mechanism with His498 acting as the catalytic base is plausible, with a reaction barrier predicted within the range of known experimental values (20–25 kcal/mol). The calculations also revealed that the catalytic reaction proceeds via a substrate-assisted mechanism, where the substrate N-acetamino group of the donor participates in the mechanism by stabilizing the leaving group. Subsequently, in 2012, Schimpl and co-worker used uridine 5′-(N-acetyl-5-thio) glucosaminyl diphosphate (UDP-5S-GlcNAc; a slowly transformed UDP-GlcNAc analogue) and proposed a second mechanism with a new set of crystal structures suggesting the α-phosphate moiety of the UDP serves as the catalytic base (Figure 1B).[14] Also their biochemical data showed that the H498F mutant preserves catalytic activity. However, in the same year Lazarus et al.[15] published another set of crystal structures and proposed a third mechanism, the so-called "proton shunting mechanism", where a water molecule serves as the catalytic base and the proton is eventually transferred to the Asp554 residue through another water molecule (Figure 1C). This study explicitly rejected α-phosphate as a candidate for the catalytic base. Thus, different mechanisms were suggested through experimental studies with a slight variation in the donor and acceptor groups.[13−15] These data provide clues as to which of the possible OGT catalytic mechanisms is correct, but none of them identify the actual process and hence it remains unclear. In our recent quantum mechanics/molecular mechanics (QM/MM) study, we modeled the GlcNAc transfer reaction that uses His498 as the catalytic base.[16] In order to investigate the OGT catalytic mechanism, the other two proposed mechanisms that employ different catalytic bases were modeled by simulating possible reaction pathways using hybrid QM/MM Car–Parrinello molecular dynamics together with the string method. The string method (STM) gives the minimum-free-energy paths (MFEP) along a set of collective reaction coordinates.[17,18] A variant of it[19] was successfully used in the study of various reaction mechanisms of enzymatic reactions including, for example, hydride transfer[20] and phosphate hydrolysis.[21,22] STM provides a more realistic description of reaction pathways than widely used static

approaches, including the potential energy surface scan[16] or nudged elastic band (NEB) methods,[23] as it does not suffer from trapping the reactant, product, and intermediate states in local minima with higher energies than the correct ones and thus artificially decreases the activation barriers found. Moreover, STM essentially provides the free-energy profiles along the found reaction pathways. Thus, all thermal effects should be properly included in the reaction description. However, the inclusion of entropic effects is rather limited in practice due to inadequate sampling (on the picosecond time scale), caused by the usage of time-consuming QM/MM methods for the potential energy calculations required during molecular dynamics simulations.

2. METHODOLOGY

To study the reaction mechanisms of the GlcNAc transfer from UDG nucleotide donor to −OH of the Ser21 acceptor, a model system was designed from the enzyme and peptide. This model was partitioned into a quantum region (QM region) closely representing the reaction mechanism. All the steps involved from model design in generating the reaction profile are described below.

2.1. Model Preparation and Molecular Mechanics Equilibration Using AMBER. Model preparation started with the human OGT crystal structure of 3TAX[24] (1.88 Å, with UDP and CKII peptide but without GlcNAc) and 4GYY[15] (1.85 Å, with UDP-5S-GlcNAc and CKII peptide with de-OH Ser21). First of all, the missing two loops of 3TAX were modeled through homology modeling using MODELLER.[25] Then from the crystal structures overlay, the UDP-5S-GlcNAc from 4GYY was transferred to 3TAX to make a Michaelis complex (MC) with h-OGT, UDP-GlcNAc, and the CKII peptide in the final ternary structure. The sulfur of UDP-5S-GlcNAc was replaced with oxygen to create a natural substrate for the OGT catalysis. All X-ray 3TAX water molecules were retained except for those having steric clashes with UDP-GlcNAc and the modeled missing loop. In the final ternary Michaelis complex of OGT, hydrogen atoms were added, and the protonation states of all residues were carefully monitored using the Maestro protein preparation wizard.[26−32] The protonation states of the residues were also cross-checked with PROPKA.[33,34] The hydrated structure was solvated in a rectangular box, heated, and equilibrated for 1.2 ns at 300 K and 1 bar pressure. The classical molecular dynamics simulations were performed employing an AMBER99SB force field using AMBER12 software.[35]

2.2. Ser21 Conformation in Crystal Structures and Possible Pathways. Close inspection of the catalytic sites of

3TAX, 4AY6, and 4GYW PDB structures reveal that each proposed mechanism requires a different orientation of the Ser-OH group for reactant and product formation (Figure 2A).
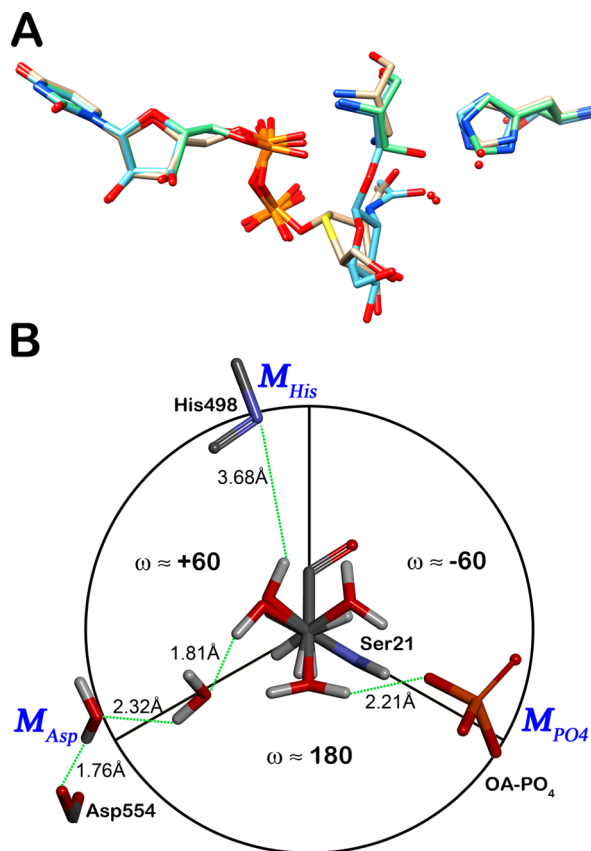
Figure 2. (A) Superimposition of substrates in the active site of high resolution X-ray structures. 3TAX (green);[13] 4AY6 (brown);[14] 4GYW(cyan);[15] (B) Schematic depiction of proposed pathways in relation to the torsion angle ω (C−Cα−Cβ−Oγ). Only a selected part of His498, PO$_4$-UDG, and Asp554 is shown for clarity. Distances of interacting atoms upon modeling are shown with dotted lines (all in Å).

This suggests that the change in the Ser21 torsion angle (ω) along the Cα−Cβ bond may give rise to all three of the proposed mechanisms (Figure 2B). The conformation of Ser21 is +*gauche* in 3TAX. Hence, we considered the same conformation for exploring the mechanism using Asp554 as the ultimate proton acceptor. However, in the product, the Ser21 was found to be in a *trans* conformation. Hence the same was considered for the mechanism using α-PO4 as the acceptor (Figure 2B). In the mechanism using His498 as the catalytic base, the Ser21 is in a +*gauche* conformation, as was already considered in our previous study.[16]

2.3. Definition of Quantum and Molecular Mechanics Regions. The AMBER equilibrated structure was partitioned in the quantum mechanics (QM) and molecular mechanics (MM) regions. The QM region includes all the essential residues for carrying out the reaction. Two partitioned regions were used to design models with a small and large QM region to study two different reaction mechanisms. The small QM region was sufficient to accommodate all the relevant atoms to study the mechanism of α-phosphate acting as a catalytic base. However, a larger QM region was needed for study of the mechanism that includes distant Asp554 as a catalytic base. The

rationale for using two different partitioned regions was to save computational time for quantum calculations. From now onward, the mechanisms under investigation in this study are referred to as mechanism−PO4 ($\mathbf{M_{PO4}}$) and mechanism−Asp ($\mathbf{M_{Asp}}$) for the proposed second and third mechanism, respectively (Figure 2B). The QM region for the $\mathbf{M_{PO4}}$ and $\mathbf{M_{Asp}}$ models consist of 103 and 146 atoms (including dummy atoms), respectively. In CPMD, dummy atoms were set to be the hydrogen atoms added to cap the QM/MM boundary. The amino acid residues common to both types of partitioning are His498, Gln839, Lys842, Thr922, and Methyl-DP-GlcNAc from UDP-GlcNAc, Ser21 from CKII peptide, and four oriented water molecules (Figure 3A). The extra molecules present in the larger model were Asp554 and Thr921 from OGT, Val20, and Ser22 from peptide CKII and a total of five water molecules (Figure 3B). The five quantum water molecules present in both types of QM regions are labeled as QMW730−734. The corresponding X-ray water molecules to QM waters in the 3TAX structure are as follows; QMW730, QMW732, and QMW733 are HOH260, HOH4, and HOH1082 from chain A, whereas QMW731 and QMW734 are HOH365 from chain B and WAT3925 from the bulk solvent, respectively. The UDP-GlcNAc was partitioned by cleaving the C5*−C4* bond, and Cα−Cβ bonds were cleaved for all the OGT amino acids except Lys842 in a small model that was cleaved at the Cδ−Cγ bond. In the large model, the amino acids Val20 and Ser22 were cleaved at the C−Cα bond, and in the small model, Ser21 was cleaved at Cα−Cβ from the CKII acceptor peptide. Dummy hydrogen atom capped the covalent bond crossing the QM/MM boundary. The QM region bounding box is 19.7 × 20.2 × 27.1 Å for the small and 19.7 × 27.4 × 27.1 Å for the large model. The MM region of the smaller model contains 11 378 solute and 80 181 solvent atoms, whereas in the larger model, the MM region contained 11 338 solute and 80 181 solvent atoms. There are in total 103 (97 + 6 dummy) and 146 (137 + 9 dummy) QM atoms for the small and large QM region, respectively.

2.4. Hybrid QM/MM Molecular Dynamics Simulation Using CPMD. The hybrid QM/MM calculations were performed on the models using the software CPMD.[36,37] The PBE functional[38] and MT pseudopotentials were used for QM calculations. The fictitious mass of wave function and time step was 600 a.u. and 5 a.u., respectively. The QM/MM calculations were started with wave function optimization, annealing (cooling of the system), and heating of the system. Systems were slowly heated to 300 K for ~2.5 ps (20 000 steps) employing two Berendsen thermostats coupled to QM and MM regions independently. After heating, the systems were equilibrated for ~3.6 ps (30 000 steps) using a Nosé−Hoover thermostat at constant volume.

2.5. String Method. The method provides a quantitative tool for comparing several different reaction mechanisms. In our work, we used the implementation provided in PMFlib[39] connected with the CPMD code that was adapted in our lab. The method is used to optimize the reaction path from an initial guess to the closest minimum free-energy path (MFEP). The path is defined as a string in the space of several collective variables (CVs) that are necessary for the proper description of all geometrical changes along the reaction. Due to the nature of the method, the path (the string) is discretized by several beads. The initial path guess was determined by three control points in the CV space connecting the initial (prereaction) and final (postreaction) state through the transition structure guess.
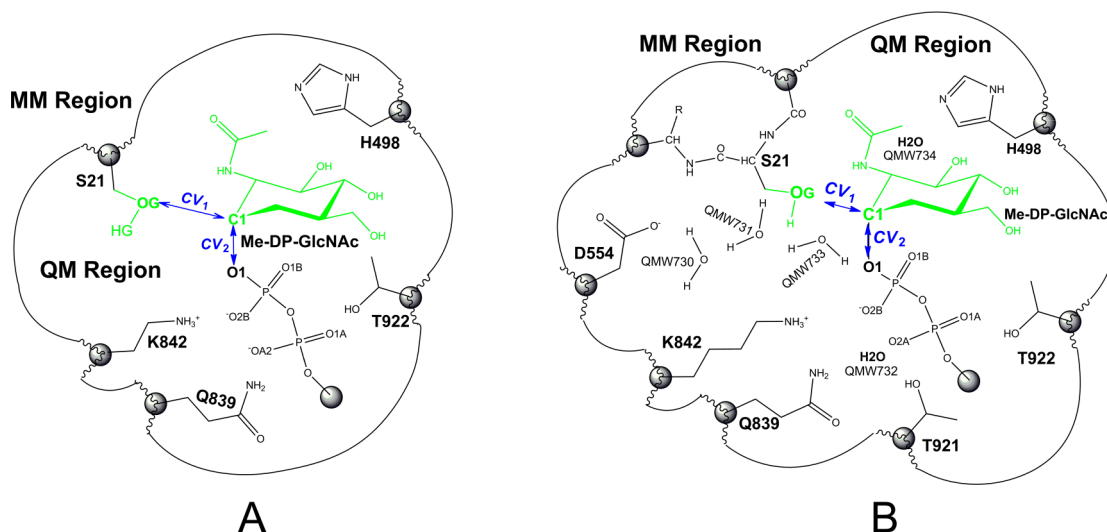
Figure 3. Schematic depiction of QM/MM partitioning with first two collective variables highlighted for (A) small QM region for M_{PO4} model and (B) large QM region for M_{Asp} model. QM water molecules are shown only in the large region for clarity. The quantum water molecules QMW732 and QMW734 are not directly involved in the reaction. Hence, they are depicted in symbolic form. The position of amino acids is adjusted to display all atoms in the 2-D space.

Used beads were uniformly spread along the interpolated path through these control points. Structures corresponding to all beads were prepared by slow driving of the system from the pre-reaction structure along the path guess. The total duration of the driving was 2.4 ps. Although we started by investigating two proposed mechanisms, we, fortunately, encountered a new mechanism that evolved during the path driving of M_{Asp}, and it is designated as M_{wPO4} (water-assisted phosphate mechanism). Used collective variables are summarized in Table 2. The first four CVs are common to all three mechanisms and describe nucleophilic attack (CV1), bond dissociation (CV2), proton transfer (CV3), and proton accepting by a catalytic base (CV4). In M_{Asp}, the remaining four CVs from CV5 to CV8 describe a proton transfer from the first water molecule to the second water molecule and from the second water molecule to the final Asp554 acceptor. In the next step, the path guess was optimized. In this method, computational demands grow linearly with the number of beads; however, it is independent of the number of CVs used for the study. This is a significant advantage over metadynamics, where the computational demands grow exponentially with the number of collective variables used. For each bead, short QM/MM molecular dynamics with CVs restrained to bead position on the path was run, and potential of mean force (PMF) was accumulated. On the basis of the accumulated PMF, the reaction path was iteratively optimized. Length of PMF accumulation step was 120 fs per bead followed by 12 fs per bead for CVs adaptation to a new bead position. The maximum STM step size was 0.005 Å for any CVs, string reparameterization and smoothing by a factor of 0.5 was done for each STM step. Collective variables were kept restrained to bead positions by a harmonic restraint with a force constant of 1000 kcal·mol^{-1}·Å^{-2}. For all the reaction mechanisms, approximately 40 iterations were performed before the path converged. Path optimization was stopped when the convergence criteria were met. Afterward, the final accumulation of PMF was acquired for 1.2 ps per bead and was used to obtain the final free-energy profile by integration. The total simulation time amounted to ~120 and ~230 ps for the small and larger QM region, respectively.

2.6. Analysis of Structures along the Reaction Path. The structures were analyzed by monitoring the collective variables for each mechanism, in particular, the Michaelis complex (MC), transition state (TS), and product complex (PC). In our previous study on the mechanism involving His498 (M_{His})[16] the N-acetyl group of glucose was suggested to stabilize the leaving group; hence, we also monitored its interaction with the leaving phosphate group for all three mechanisms. The Ser21 $C\alpha$–$C\beta$ torsion angle was monitored from the reactant to the product. The ring conformation of the saccharide (GlcNAc) was also monitored to observe any changes in the chair–skew–boat forms employing the Cremer–Pople ring-puckering parameters.[40]

3. RESULTS AND DISCUSSION

3.1. AMBER Equilibration. The initial model was compared with the AMBER-equilibrated structure to identify the overall changes in the Michaelis complex (MC) structure. No significant changes were observed in the equilibrated OGT MC structure (Figure S1). The movement of the atoms in the active site was closely inspected, and no substantial deviation from original positions was detected.

3.2. Hybrid QM/MM Molecular Dynamics Equilibration. The AMBER-equilibrated structure was partitioned into QM and MM regions having a small QM region size for M_{PO4} and large QM region size for M_{Asp}. All further calculations were performed using the hybrid QM/MM method in CPMD. These systems were optimized for a wave function, annealed, and slowly heated to 300 K in 2.5 ps and then equilibrated by molecular dynamics for 3.6 ps. M_{Asp} was derived from M_{PO4} by rotating the hydroxyl group of Ser21 toward QMW731 through a change in torsion angle during the short dynamics. After reaching the required torsion angle, the M_{Asp} system was equilibrated for ~2.5 ps. The Ser21 torsion angle (ω) for M_{Asp} is +gauche and for M_{PO4} is a trans conformation. During the equilibration, the CV distances were monitored, and the values obtained at the end of the equilibration are reported in Table 1 along with Ser21 torsion angle (ω). During the path drive of M_{Asp}, a new mechanism was found, M_{wPO4}. We assume that this

Table 1. Initial CVs and Torsion Angle (ω) Used for Path Driving Obtained in QM/MM Molecular Dynamics Equilibration[a]

	CV1	CV2	CV3	CV4	ω
M_{PO4}	3.63	1.50	1.03	1.72	175
M_{Asp}	4.47	1.41	1.01	1.96	59
M_{wPO4}[b]	3.84	1.46	0.98	3.38	−70

[a]CV values are in Å and torsion angle (ω) in degrees. [b]This mechanism was produced during the path drive of M_{Asp}.

was a consequence of restraining the distance and not the Ser21 torsion angle (ω) during the path drive. The model system for M_{wPO4} was equilibrated, and the torsion angle (ω) was observed to be in a −*gauche* conformation.

3.3. Path Driving and Collective Variable Evolution during Optimization. The reaction paths from MC to the product complex were derived for the mechanisms under investigation. The CVs used to monitor the reaction mechanism are defined in Table 2. Beads were generated along the reaction path connecting the reactant to the product through the intermediates. During the M_{Asp} path driving, M_{wPO4} was encountered, where the −OH of Ser21 moves away from QMW730 (pointing toward Asp554 in M_{Asp}) toward O1A−PO4, and a proton was transferred from Ser21 to the α-phosphate via the QMW733 water molecule. Although this mechanism is similar to M_{PO4}, it differs in the way the proton is transferred. In M_{PO4}, the proton is directly transferred to the α-phosphate (O1A), whereas in M_{wPO4}, the proton transfer is water-assisted. Before the path driving, M_{wPO4} was equilibrated for 0.6 ps. The number of beads generated for M_{Asp} is 41, and for M_{PO4} and M_{wPO4}, it was 21 beads. The C1−OG distance in MC for M_{PO4} is 3.6 Å. Hence, 21 beads were sufficient to sample the reaction path. However, in M_{Asp} the reactant C1−OG distance is 4.4 Å, and therefore, 41 beads were generated to sample the path, which involves the passage/shunting of proton from Ser21 to the distantly located Asp554 via two water molecules. After the path driving for each mechanism, restart files corresponding to each bead were generated and used to optimize the path in multiple iterations. Approximately 40 iterations were performed for each mechanism before the path converged, and for each iteration, the free-energy profile was obtained. The bead space is defined as the distribution of beads generated, between 0 to 1, where 0 represents the MC and 1 the product.

The evolution of CVs (Figure S2−S4) and free-energy profile (Figure S5−S7) for each iteration during the optimization for all the three mechanisms is provided in the Supporting Information (SI). These graphs suggest that the CVs in the reaction path fluctuate, especially near the transition state, and the reaction path gets progressively optimized. Even the free-energy profile fluctuates, and the lowest energy curve is, however, not the last iteration of the optimization. With M_{PO4}, the product was energetically more stable than the reactant in eight iterations, suggesting an exoergic reaction (Figure S5). Compared to the first iteration, the optimized path (last iteration) has a TS free-energy barrier and product more stable by approximately 20.0, 30.0, and 10.0 kcal/mol for M_{PO4}, M_{Asp} and M_{wPO4}, respectively.

3.4. Important Reaction Events along the Equilibrated Reaction Path. In our previous study investigating the mechanism utilizing His498 as the catalytic base, we showed that the order of events associated with the *O*-GlcNAc
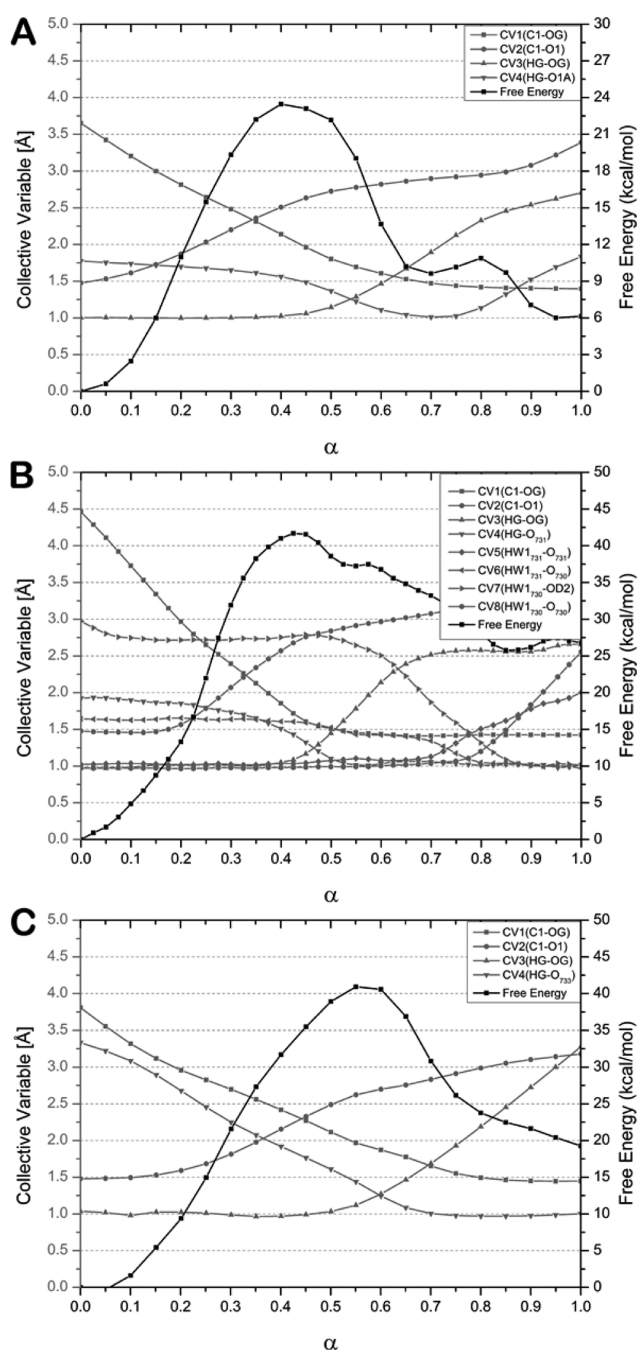
Table 2. List of Collective Variables (CVs) and Monitored Torsion Angles (TA) in Michaelis Complex (MC), Transition State (TS), and Product Complex (PC) of all the Three Mechanisms[a]

		mechanism–PO4			mechanism–Asp			mechanism–wPO4	
	CVs descriptions	ES	TS	PC	ES	TS	PC	ES	TS	PC
CV1	C1–OG	3.65 (0.02)	2.15 (0.02)	1.41 (0.02)	4.46 (0.02)	1.72 (0.03)	1.43 (0.02)	3.56 (0.02)	1.97 (0.03)	1.44 (0.01)
CV2	C1–O1	1.47 (0.02)	2.52 (0.02)	3.22 (0.03)	1.48 (0.02)	2.69 (0.03)	3.15 (0.03)	1.48 (0.02)	2.63 (0.03)	3.18 (0.02)
CV3	OG–HG	1.00 (0.01)	1.03 (0.01)	2.63 (0.01)	0.99 (0.01)	1.08 (0.01)	2.56 (0.01)	1.01 (0.01)	1.11 (0.01)	3.28 (0.01)
CV4	HG–O1A/O731/O733/	1.77 (0.02)	1.56 (0.02)	1.70 (0.02)	1.92 (0.02)	1.43 (0.02)	1.01 (0.01)	3.33 (0.02)	1.44 (0.02)	1.01 (0.01)
CV5	(HW1731–O731)				1.02 (0.01)	1.03 (0.01)	1.62 (0.02)			
CV6	(HW1731–O730)				1.65 (0.03)	1.61 (0.02)	1.03 (0.01)			
CV7	(HW1730–OD2)				2.97 (0.02)	2.77 (0.02)	1.08 (0.01)			
CV8	(HW1730–O730)				0.99 (0.01)	0.99 (0.01)	1.49 (0.02)			
	TA descriptions									
ω	C–Cα–Cβ–Oγ	190.56 (9.05)	191.36 (9.67)	210.67 (10.89)	67.77 (6.27)	329.04 (12.61)	146.73 (18.62)	304.81 (7.98)	302.91 (17.10)	276.52 (10.56)
	H2–C2–N2–HN2	190.07 (21.23)	201.36 (10.84)	192.20 (12.32)	232.17 (9.26)	185.98 (9.37)	184.00 (8.57)	161.63 (18.01)	199.04 (9.88)	193.91 (10.38)

[a]The average CVs distances are in angstrom and torsion angles (TA) in degree with their standard deviation in parentheses.

glycosidic bond formation is nucleophilic attack, bond dissociation, and proton transfer.[16] Here we compared the order of occurrence of these events in the other three mechanisms through molecular dynamics. The CVs after 1.2 ps of equilibration after path optimization is shown in Figure 4.

Mechanism−PO4. Here the reacting species are in proximity, hence the reaction starts very early in the bead space (Figure 4A). The reaction proceeds with the C1−OG distance getting closer and as soon as they reach 3.2 Å (the sum of the vdw radii for C1 and OG), the C1−O1 bond begins to elongate. The C1−O1 bond continues to elongate and very

Figure 4. Optimized collective variables (CVs) and free-energy profile along the reaction path. The reaction coordinate α changes from the Michaelis complex, ($\alpha = 0$) to the product complex ($\alpha = 1$) for (A) M_{PO4}; (B) M_{Asp}; and (C) M_{wPO4}.

soon around the 0.3 bead space (before reaching the TS) the bond dissociates, leaving behind an oxocarbenium ion. Once the C1−OG distance is around 2.2 Å, protonated Ser21 initiates nucleophilic attack to an oxocarbenium ion (C1). On the other hand, the OG−HG bond elongates, and the HG−O1A distance shortening is marked as the beginning of the proton transfer. The exchange of a proton from OG−HG to O1A occurs after the 0.65 bead space. The proton transfer is in sync with the formation of the C1−OG glycosidic bond. Here the last event is the formation of the C1−OG glycosidic bond occurring around the 0.8 bead space. The relative order of the different reaction events are nucleophilic attack (leading to bond dissociation), proton transfer, and immediate glycosidic bond formation.

Mechanism−Asp. This mechanism is quite complex in contrast to M_{PO4}, because, in total, there are three proton transfers in addition to the formation of the glycosidic bond. The reaction begins once C1−OG reaches the sum of their vdw radii (a distance of 3.2 Å), which occurs at around 0.18 in the bead space (Figure 4B). The reaction is initiated by the elongation of the C1−O1 bond resulting in bond dissociation, leaving behind an oxocarbenium ion (C1) and uridine diphosphate (UDP). The next step is a nucleophilic attack from the protonated Ser21 to C1, proton transfer from Ser21 to QMW731, and simultaneous formation of the C1−OG glycosidic bond. In the latter part of the reaction, a proton is transferred via two water molecules to the Asp554. In this case, the order of reaction events is nucleophilic attack, first proton transfer (Ser21 to QMW731), glycosidic bond formation, and later transfer of the proton from the QMW731 water to Asp554 via the QMW730 water molecule. The reaction events support the mechanism, suggesting a shunting of a proton from Ser21 to Asp554 via two water molecules.[15]

Mechanism−wPO4. This mechanism is very similar to M_{PO4}, the only difference being in the torsion angle (ω) of Ser21, which is −*gauche*, in this case. The proton donor and acceptor groups are positioned in proximity for the reaction to occur (Figure 4C). On approaching the C1−OG distance of 3.22 Å, the C1−O1 bond starts to elongate quickly and soon dissociates. The protonated Ser21 starts its nucleophilic attack on oxocarbenium ion C1, and the proton is transferred to the oxygen of QMW733. Further, this proton is transferred to O1A through the water molecule (QMW733) and the C1−OG glycosidic bond is formed. This mechanism also turned out to follow the same order of events as the reaction mechanisms M_{PO4} and M_{Asp}.

The order of events suggests that in all three mechanisms under investigation, the *O*-GlcNAc transfer and glycosidic bond formation is a dissociative S_N2 type reaction, through an oxocarbenium species. This ion is suggested to be positively charged and stabilized through resonance and is the center for the nucleophilic attack through the protonated Ser21. The relative order of the different reaction events in all the mechanisms are nucleophilic attack, which leads to bond dissociation, proton transfer, and immediate glycosidic bond formation.

3.5. Structural Analysis of Important Reaction Events. In-depth analysis of the structural details of the reacting species is important to see the various interactions stabilizing the reacting species as the reaction proceeds. The structures of important reaction events are given in Figure 5, obtained from the trajectory of the equilibrated reaction path after path optimization. The key distances for the MC, TS, and PC
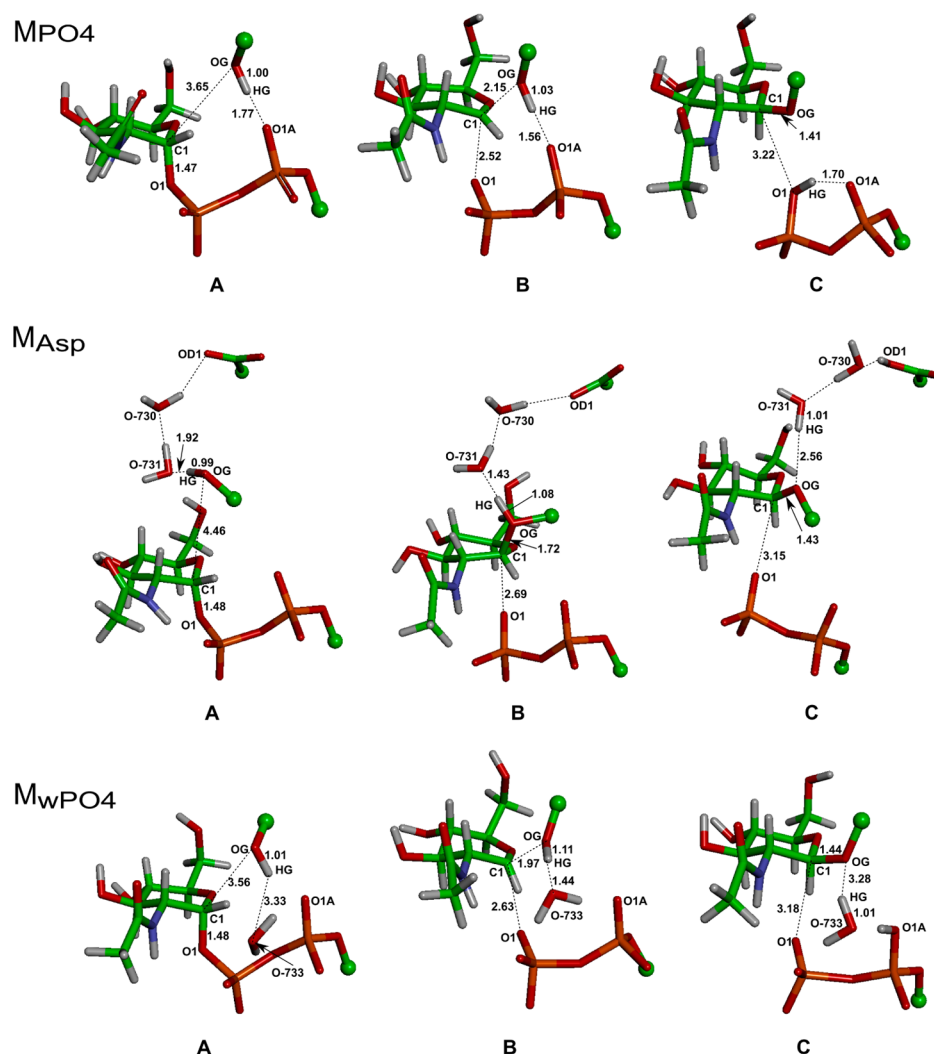
Figure 5. Selected snapshots from the STM trajectory along the optimized reaction pathways representing (A) Michaelis complex, (B) transition state and (C) product complex. Green spheres indicate methyl group of Ser21 and UDG present in M_{PO4}, M_{Asp}, and M_{wPO4}, and Asp554 in M_{Asp}. The average CV distances shown are in Å.

together with a standard deviation are given in Table 2 for all three mechanisms.

Mechanism—PO4. In this mechanism, the reacting molecules of the Michaelis complex are positioned in close proximity in the space at a very appropriate reaction distance, such as C1−OG at ~3.7 Å and HG−O1A distance of ~1.78 Å (Figure 5, Table 2). The torsion angle (ω) of Ser21 is in a *trans* (190° ± 9) conformation and the pyranose ring conformation of the reactant is close to $^4C_1$ chair form with a subtle distortion from the perfect chair form. The reaction starts with the C1−O1 glycosidic bond elongation when C1−OG approaches ~3.2 Å (the sum of their vdw radii). The C1−O1 bond elongation continues and dissociates as the C1−OG distance shortens before reaching the TS. After glycosidic bond cleavage, the GlcNAc ring gradually shifts into the $^2H_3$, E_3 and other skewed forms (falling between the $^2H_3$ and E_3 forms) before reaching and leaving the TS. A total of three beads showing the maximum distortion in the ring conformation immediately precede and follow the TS. Their puckering parameters are (φ = 167°, θ = 68°), (φ = 149°, θ = 51°), and (φ = 157°, θ = 75°) (Figure S8). A reduction by ~0.15 Å was also observed for the C1−O5 bond length. At the TS, the C1−OG distance is ~2.16 Å and is characterized by the nucleophilic attack by protonated

Ser21 at the oxocarbenium ion (C1). Later, the proton is transferred to the α-phosphate with an HG−O1A distance of 1.25 Å, and the glycosidic bond is formed immediately. The leaving group diphosphate uridine (O1B, O2B, O2A) is stabilized by Lys842, Thr922, and QMW732. The involvement of the *N*-acetyl group in stabilizing the leaving group is less pronounced here than was observed in M_{His} in our previous study.[16] Here the N−H of the *N*-acetyl group mostly interacts with O1B throughout the reaction, with the distance ranging between 2.0 to 3.0 Å; however, when approaching the TS, N−H is closer to O1. The torsion angle (ω) of Ser21 in the product is 210° ± 11.

Mechanism—Asp. This mechanism is the longest of all three mechanisms under investigation in terms of the number of events because a total of three proton transfers occur to complete the reaction. In the reactant (MC), the Ser21 torsion angle (ω) is +*gauche* (68° ± 6), and the ring conformation of GlcNAc is in $^4C_1$ chair form. The reaction starts with a C1−OG distance of ~4.5 Å (Figure 5, Table 2), and as they reach the sum of their vdw radii (3.2 Å), C1−OG bond elongation quickens and continues, leading to bond cleavage and the formation of the oxocarbenium ion (C1). This ion initiates a conformational change in the ring, and C1 shifts into a planar

conformation, which facilitates closer contact with OG. Nucleophilic attack from protonated Ser21 to the oxocarbenium C1 is the start of the catalysis. Proton transfer initiates at the TS and the glycosidic bond is formed immediately after proton transfer. The GlcNAc ring conformation in four beads preceding the TS fall between the E_3 and $^4H_3$ ring conformation, whereas at the TS, it is close to a $^4H_3$ half-chair form with puckering parameters of $\varphi = 220°$ and $\theta = 49°$. The maximum distortion in the ring conformation was observed for the bead immediately adjacent to the TS with $\varphi = 210°$, $\theta = 75°$ (Figure S8). Until the proton is transferred to Asp554, the leaving diphosphate uridine group is stabilized by Lys842, Thr921, CKII peptide−N−H, and Gln839. There is constant interaction between the QMW733, QMW734 molecules and the Lys842, Glu839, and O2A of PO4. O1A interacts with the peptide backbone throughout the reaction. The N−H of the N-acetyl group fluctuates toward and away from the phosphate group throughout the reaction; however it stabilizes the TS by interacting with O1 at a distance of ~2.2 Å, although it is much closer to O1B. At the end of the reaction, the H−N of the N-acetyl group interacts with QMW733, which further interacts with O1A and O1B. The N−H⋯O1 distance in the product complex is ~3.9 Å. A CH⋯O-type weak interaction is possible between O1 and H1 at a distance of ~2.2 Å. Moreover, the other oxygen atoms linked to the phosphate are stabilized by residues in the vicinity or via quantum water. The two quantum water molecules (QMW731 and QMW730) are involved in shunting the proton from Ser21 to Asp554. Before the first proton transfer occurs, the QMW731 water molecule interacts with the O6H of GlcNAc until the C1−O1 distance reaches ~2.8 Å. In this mechanism, proton transfer starts near the TS. At a C1−O1 distance of ~2.8 Å, QMW731 starts interacting with Ser21−HG, however, QMW731 is dynamic, and its oxygen also interacts with O6H. QMW731 serving as the catalytic base accepts the HG proton and keeps it for a long time until it transfers to the second water molecule (QMW730). During this time, both the water molecules (QMW731 and QMW730) reorient and slowly align linearly to form an optimal H−bond from the QMW731 water to QMW730 and then QMW730 with the OD2 of Asp554. The second proton transfer is marked by a proton transfer from QMW731 to QMW730 and then the transfer to Asp554 occurs almost immediately. The Ser21 torsion angle (ω) in the product complex is $144° \pm 9$.

Mechanism−wPO4. The reaction starts with the Michaelis complex having a C1−OG distance of ~3.6 Å (Figure 5). The torsion angle (ω) of Ser21 is −*gauche* ($304° \pm 8$). In this case, the proton transfer is water-assisted via QMW733 to its acceptor O1A, which is very close to Ser21-HG. The reaction path progresses with the decrease in the C1−OG distance and increase in the HG−O1A distance, bringing OG close to QMW733. The starting conformation of GlcNAc is $^4C_1$ with a small deviation from its perfect chair form, which undergoes ring conformational changes when the C1−O1 distance reaches ~2.0 Å. C1−O1 bond cleavage is observed just before the TS, leaving an oxocarbenium ion (C1). The CVs for the MC, TS, and PC are given in Table 2. The beads approaching and leaving the TS shift into the E_3 and $^4H_3$ conformation, respectively (Figure S8). The TS is in envelope E_3 form having a puckering parameter of $\varphi = 178°$; $\theta = 48°$. At the TS, nucleophilic attack is followed by proton transfer from Ser21 to QMW733. This water molecule is in close vicinity to O1A. Hence, the proton is held with QMW733 for a while and then

transferred to O1A. After the proton transfer and glycosidic bond formation, GlcNAc returns to its $^4C_1$ chair conformation. The TS of this mechanism displays many interactions, such as QMW733 interacting with O1A, O1B and Ser21−HG. O1B also interacts with Lys842, O2B with Thr921, O2A with Gln839 and O1 with H1 through a CH⋯O interaction. The N−H of the N-acetyl group interacts with the O1 more closely than with O1B before reaching the TS. At the TS and the later stages until product formation, the N−H⋯O1 distance ranged between ~2.0 to 2.5 Å. The torsion angle (ω) of Ser21 in the product complex is −*gauche* ($276° \pm 10$).

In the three mechanisms, the starting C1−OG distance varies; however, for all of them, the C1−O1 bond elongation starts at almost the same C1−OG distance (~3.2 Å). The structural details near the TS are also similar except for $\mathbf{M_{PO4}}$. In this case, at the TS, a difference between CV1 and CV2 is smallest, and the C1−OG and C1−O1 distances are 2.14 and 2.51 Å respectively, exhibiting a dissociative character (Table 2). Ring conformational change was observed in all three mechanisms. The reactant (MS) and product remain in the $^4C_1$ conformation, with a small deviation from its perfect $^4C_1$ chair form. During the reaction, GlcNAc undergoes ring conformation changes and shifts into various envelope and half-chair forms, clearly visible while approaching or leaving the TS. These various forms help to position the oxocarbenium closer to the Ser21 nucleophilic center and are marked by a decrease in the bond length of O5−C1. Also, the oxocarbenium ion is proposed to increase the charge at the anomeric carbon through charge distribution. The atoms linked to the anomeric center become coplanar and have sp^2-like characteristics. The N-acetyl group interacts with the O1 and O1B of the leaving UDP with the distance varying between ~2.0 to 3.5 Å.

3.6. Energy Profile of Equilibrated Reaction Path. The free-energy profile for the equilibrated reaction path for all three mechanisms was extracted. The shape of the free-energy reaction profiles differ for all the mechanisms, and all are endoergic in nature (Figure 6). The relative free-energy values for the Michaelis complex, transition state, and product complex in kcal/mol are given in Table 3 for all three mechanisms under investigation. It is worth mentioning that the starting conformation of the Ser21 residue may influence the height of the reaction barrier as the reactant complexes may
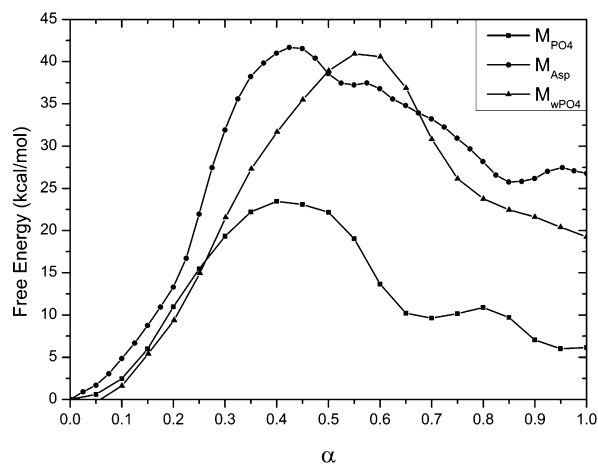
Figure 6. Comparison of free-energy profiles of three optimized reaction pathways. The reaction coordinate α changes from the Michaelis complex ($\alpha = 0$) to the product complex ($\alpha = 1$).

Table 3. Free Energy Value in kcal/mol at Different Events along Reaction Path Relative to the MC

	MC	TS	first Int Min[a]	2nd TS	PC
M_{PO4}	0.00	23.46	9.63	10.88	6.01
M_{Asp}	0.00	41.69	37.24	37.48	25.76
M_{wPO4}	0.00	40.93	-	-	19.25

[a]First intermediate minima.

have different potential energy. To investigate this phenomenon, we have calculated the free energy of the Ser21 side chain rotation in the reactant complex. We have found out that the energy difference between the rotamers is below 1 kcal/mol, which is significantly less than the difference between the observed free-energy reaction profiles (for more details see SI, Figure S9).

Mechanism−PO4. The free-energy reaction profile rises from the beginning (Michaelis complex) up to 23.5 kcal/mol at the TS and later after crossing the TS barrier, the energy decreases (Figure 6). The CV distances at the TS are given in Table 2. A small local energy minimum is observed at the first intermediate, of ~9.6 kcal/mol. This intermediate is characterized by a proton transfer to the α-phosphate and the formation of a glycosidic bond. This is followed by a very small energy barrier of ~1.0 kcal/mol and jumps to the final products, where the Ser21 proton is transferred from the α-phosphate (O1A) to the β-phosphate (O1), and the final reaction products are formed. This mechanism is endoergic in character, having a product free energy 6.0 kcal/mol higher than that of the MC. However, only this mechanism exhibited an exoergic character for some iterations during the optimization, where the product was found to be more stable than the reactant (Figure S5).

Mechanism−Asp. The shape of the free-energy reaction profile consists of the TS and one local minimum and maximum (2nd TS) and is similar to M_{PO4}. The free-energy reaction profile rises from the beginning (Michaelis complex) reaching the TS barrier of ~41.7 kcal/mol and then decreases to the first local minimum corresponding to an intermediate structure (Figure 6). The CV distances at the TS are given in Table 2. In this structure, the Ser21 proton is transferred to the QMW731 water molecule functioning as a general base and a new Ser21−GlcNAc glycosidic bond is formed. A second local maximum (2nd TS) represents the reorientation of the water molecules leading to the second and third proton transfer to the OD2 oxygen of Asp554 to form the final product. The lowest minimum energy corresponds to the proton transfer to the Asp554 residue and represents the product structure, which is ~26.0 kcal/mol higher than that of the reactants. The small rise in the energy after product formation is because of the increased distance between the QMW730 water molecule and Asp554.

Mechanism−wPO4. The free-energy profile of this reaction has one TS barrier of ~40.9 kcal/mol and resembles M_{PO4} (Figure 6). The energy rises as the reaction proceeds and after crossing the TS barrier, the product is formed which is ~19.00 kcal/mol higher than the reactant. However, the difference in the TS barrier of M_{PO4} and M_{wPO4} is ~17.0 kcal/mol. This might suggest that the water-assisted proton transfer is energetically less favorable than M_{PO4} and is less likely to occur. Alternatively, another explanation might be that the proton in the product is with O1A but strongly interacts with the oxygen of QMW733 and shows a tendency to revert back,

resulting in an energetically less stable product. The comparison of free-energy reaction profiles for all three mechanisms displays differences in their shape and the height of their TS barrier. The TS barriers in order from highest to lowest are M_{Asp}, M_{wPO4}, and M_{PO4}. With M_{Asp}, the TS barrier is highest, and product least stable compared to the other two mechanisms. M_{wPO4}, which is the water-assisted model of M_{PO4}, has a TS barrier which is almost double that of M_{PO4}, suggesting transfer of the proton via the water molecule is not favored compared to direct transfer. The free energy of the product in M_{PO4}, M_{wPO4}, and M_{Asp}, having values of 6.0, 19.3, and 25.8 kcal/mol respectively, also corresponds to the decreasing order of product stability (Table 3). In M_{PO4} and M_{wPO4}, direct neutralization of the created phosphate anion is possible through the charged residue present in the vicinity. In our previous study on the first mechanism using His498 as the catalytic base, the activation energy was calculated to be ~20.0 kcal/mol.[16] It seems that the energy at the TS for the mechanism using His498 (the first proposed mechanism)[13] and α-phosphate (second proposed mechanism)[14] as the catalytic base is very close, but this difference could be the result of the different methodology used to study the reaction mechanism.[16]

4. CONCLUSIONS

In this study, we investigated the two recently proposed catalytic mechanisms for OGT together with a new mechanism found during this study. The results presented here were obtained by hybrid QM/MM Car−Parrinello molecular dynamics employing the string method for free energy estimation. The string method was able to optimize the reaction path efficiently for all three mechanisms studied in this work, and it was able to find the most probable mechanisms. All three reaction mechanisms share several common features. In all cases, the reaction starts with the nucleophilic attack of Ser21 hydroxyl to the C1 of GlcNAc leading to bond dissociation, followed by proton transfer from the Ser21 to a base acceptor and immediate formation of the glycosidic bond. Most of the simulation time, the reactant and product remain in the $^4C_1$ conformation, with a small deviation from its perfect chair form. As the reaction progress from the reactant to the product state, GlcNAc undergoes changes in its ring conformation and shifts into various envelope and half-chair forms. Despite the varying C1−OG bond length in the reactants of the different mechanisms, C1−O1 bond elongation begins when the C1−OG distance is ~3.2 Å. In most cases, the glycosidic bond (C1−O1) cleavage triggers a ring conformational change and it is more clearly visible when approaching or leaving the TS. Structural details for M_{PO4} show the transition state has a slightly dissociative character, having similar distances for C1−O1 and C1−OG. In the other two mechanisms, this difference is larger. The calculated free-energy reaction profiles suggest that the M_{PO4} mechanism is favorable. The reaction mechanism M_{PO4} has the lowest rate-limiting free-energy barrier (23.5 kcal/mol) of the three mechanisms modeled. The calculated barriers for the M_{Asp} and M_{wPO4} mechanisms are 41.7 and 40.9 kcal/mol, respectively. The most and least stable product complex is for M_{PO4} and M_{Asp}, respectively. Another interesting thing is that the Ser21 torsion angle (ω) *trans* conformation is only retained throughout the reaction from the MC to PC in M_{PO4}, which is consistent with all known post-translational X-ray structures.[15] In contrast, M_{Asp} and M_{wPO4} require a *gauche* conformation for the substrate to approach the donor correctly. Thus, an

additional conformation change from the *gauche* to the *trans* conformation would have to occur during the reaction. Simulations of the different reaction mechanisms of OGT provide new insight into the catalytic reaction of OGT and may be used in the rational drug design of transition state analog inhibitors with potential therapeutic uses.

ASSOCIATED CONTENT

Ⓢ Supporting Information

Additional data as referenced in the text. This material is available free of charge via the Internet at http://pubs.acs.org.

AUTHOR INFORMATION

Corresponding Author

*E-mail: jkoca@chemi.muni.cz.

Present Address

◆On leave of absence from the Institute of Chemistry, Slovak Academy of Sciences, Bratislava, Slovakia

Author Contributions

‖M.K. and S.K. contributed equally. The manuscript was written through contributions of all authors. All authors have given approval to the final version of the manuscript.

Notes

The authors declare no competing financial interest.

ACKNOWLEDGMENTS

REFERENCES

(1) Tvaroska, I. Atomistic Insight into the Catalytic Mechanism of Glycosyltransferases by Combined Quantum Mechanics/molecular Mechanics (QM/MM) Methods. *Carbohydr. Res.* **2015**, *403*, 38−47.
(2) Breton, C.; Fournel-Gigleux, S.; Palcic, M. M. Recent Structures, Evolution and Mechanisms of Glycosyltransferases. *Curr. Opin. Struct. Biol.* **2012**, *22*, 540−549.
(3) Lairson, L. L.; Henrissat, B.; Davies, G. J.; Withers, S. G. Glycosyltransferases: Structures, Functions, and Mechanisms. *Annu. Rev. Biochem.* **2008**, *77*, 521−555.
(4) Varki, A.; Etzler, M. E.; Cummings, R. D.; Esko, J. D. Discovery and Classification of Glycan-Binding Proteins. In *Essentials of Glycobiology*, 2nd ed.; Varki, A., Cummings, R. D., Esko, J. D., Freeze, H. H., Stanley, P., Bertozzi, C. R., Hart, G. W., Etzler, M. E., Eds.; Cold Spring Harbor Laboratory Press: Cold Spring Harbor, New York, 2009.
(5) Hart, G. W.; Slawson, C.; Ramirez-Correa, G.; Lagerlof, O. Cross Talk Between O-GlcNAcylation and Phosphorylation: Roles in

Signaling, Transcription, and Chronic Disease. *Annu. Rev. Biochem.* **2011**, *80*, 825−858.
(6) Ruan, H.-B.; Singh, J. P.; Li, M.-D.; Wu, J.; Yang, X. Cracking the O-GlcNAc Code in Metabolism. *Trends Endocrinol. Metab.* **2013**, *24*, 301−309.
(7) Shafi, R.; Lyer, S. P. N.; Ellies, L. G.; O'Donnell, N.; Marek, K. W.; Chui, D.; Hart, G. W.; Marth, J. D. The O-GlcNAc Transferase Gene Resides on the X Chromosome and Is Essential for Embryonic Stem Cell Viability and Mouse Ontogeny. *Proc. Natl. Acad. Sci. U.S.A.* **2000**, *97*, 5735−5739.
(8) Webster, D. M.; Teo, C. F.; Sun, Y.; Wloga, D.; Gay, S.; Klonowski, K. D.; Wells, L.; Dougan, S. T. O-GlcNAc Modifications Regulate Cell Survival and Epiboly during Zebrafish Development. *BMC Dev. Biol.* **2009**, *9*, 28.
(9) Hart, G. W.; Housley, M. P.; Slawson, C. Cycling of O-Linked Beta-N-Acetylglucosamine on Nucleocytoplasmic Proteins. *Nature* **2007**, *446*, 1017−1022.
(10) Lefebvre, T. Neurodegeneration: Recall Sugars, Forget Alzheimer's. *Nat. Chem. Biol.* **2012**, *8*, 325−326.
(11) Yi, W.; Clark, P. M.; Mason, D. E.; Keenan, M. C.; Hill, C.; Goddard, W. A.; Peters, E. C.; Driggers, E. M.; Hsieh-Wilson, L. C. Phosphofructokinase 1 Glycosylation Regulates Cell Growth and Metabolism. *Science* **2012**, *337*, 975−980.
(12) Compain, P.; Martin, O. R. Carbohydrate Mimetics-Based Glycosyltransferase Inhibitors. *Bioorg. Med. Chem.* **2001**, *9*, 3077−3092.
(13) Lazarus, M. B.; Nam, Y.; Jiang, J.; Sliz, P.; Walker, S. Structure of Human O-GlcNAc Transferase and Its Complex with a Peptide Substrate. *Nature* **2011**, *469*, 564−U168.
(14) Schimpl, M.; Zheng, X.; Borodkin, V. S.; Blair, D. E.; Ferenbach, A. T.; Schuettelkopf, A. W.; Navratilova, I.; Aristotelous, T.; Albbarawi, O.; Robinson, D. A.; et al. O-GlcNAc Transferase Invokes Nucleotide Sugar Pyrophosphate Participation in Catalysis. *Nat. Chem. Biol.* **2012**, *8*, 969−974.
(15) Lazarus, M. B.; Jiang, J.; Gloster, T. M.; Zandberg, W. F.; Whitworth, G. E.; Vocadlo, D. J.; Walker, S. Structural Snapshots of the Reaction Coordinate for O-GlcNAc Transferase. *Nat. Chem. Biol.* **2012**, *8*, 966−968.
(16) Tvaroska, I.; Kozmon, S.; Wimmerova, M.; Koca, J. Substrate-Assisted Catalytic Mechanism of O-GIcNAc Transferase Discovered by Quantum Mechanics/Molecular Mechanics Investigation. *J. Am. Chem. Soc.* **2012**, *134*, 15563−15571.
(17) Weinan, E.; Ren, W. Q.; Vanden-Eijnden, E. String Method for the Study of Rare Events. *Phys. Rev. B* **2002**, *66*, 052301.
(18) Maragliano, L.; Fischer, A.; Vanden-Eijnden, E.; Ciccotti, G. String Method in Collective Variables: Minimum Free Energy Paths and Isocommittor Surfaces. *J. Chem. Phys.* **2006**, *125*, 024106.
(19) Weinan, E.; Ren, W. Q.; Vanden-Eijnden, E. Finite Temperature String Method for the Study of Rare Events. *J. Phys. Chem. B* **2005**, *109*, 6688−6693.
(20) Lans, I.; Medina, M.; Rosta, E.; Hummer, G.; Garcia-Viloca, M.; Lluch, J. M.; Gonzalez-Lafont, A. Theoretical Study of the Mechanism of the Hydride Transfer between Ferredoxin-NADP(+) Reductase and NADP(+): The Role of Tyr303. *J. Am. Chem. Soc.* **2012**, *134*, 20544−20553.
(21) Rosta, E.; Nowotny, M.; Yang, W.; Hummer, G. Catalytic Mechanism of RNA Backbone Cleavage by Ribonuclease H from Quantum Mechanics/Molecular Mechanics Simulations. *J. Am. Chem. Soc.* **2011**, *133*, 8934−8941.
(22) Ganguly, A.; Thaplyal, P.; Rosta, E.; Bevilacqua, P. C.; Hammes-Schiffer, S. Quantum Mechanical/Molecular Mechanical Free Energy Simulations of the Self-Cleavage Reaction in the Hepatitis Delta Virus Ribozyme. *J. Am. Chem. Soc.* **2014**, *136*, 1483−1496.
(23) Henkelman, G.; Jonsson, H. Improved Tangent Estimate in the Nudged Elastic Band Method for Finding Minimum Energy Paths and Saddle Points. *J. Chem. Phys.* **2000**, *113*, 9978−9985.
(24) Jiang, J.; Lazarus, M. B.; Pasquina, L.; Sliz, P.; Walker, S. A Neutral Diphosphate Mimic Crosslinks the Active Site of Human O-GlcNAc Transferase. *Nat. Chem. Biol.* **2012**, *8*, 72−77.

(25) Sali, A.; Blundell, T. Comparative Protein Modeling by Satisfaction of Spatial Restraints. *J. Mol. Biol.* **1993**, *234*, 779−815.

(26) Sastry, G. M.; Adzhigirey, M.; Day, T.; Annabhimoju, R.; Sherman, W. Protein and Ligand Preparation: Parameters, Protocols, and Influence on Virtual Screening Enrichments. *J. Comput. Aided Mol. Des.* **2013**, *27*, 221−234.

(27) *Schrodinger Suite 2013 Protein Preparation Wizard*; Schrodinger, LLC: New York, NY, 2013.

(28) *Epik*; Schrodinger, LLC: New York, NY, 2013.

(29) *Impact*; Schrodinger, LLC: New York, NY, 2013.

(30) *Prime*; Schrodinger, LLC: New York, NY, 2013.

(31) *Maestro*; Schrodinger, LLC: New York, NY, 2013.

(32) *Schrodinger Suite*; Schrodinger, LLC: New York, NY, 2013.

(33) Sondergaard, C. R.; Olsson, M. H. M.; Rostkowski, M.; Jensen, J. H. Improved Treatment of Ligands and Coupling Effects in Empirical Calculation and Rationalization of pK(a) Values. *J. Chem. Theory Comput.* **2011**, *7*, 2284−2295.

(34) Li, H.; Robertson, A. D.; Jensen, J. H. Very Fast Empirical Prediction and Rationalization of Protein pKa Values. *Proteins* **2005**, *61*, 704−721.

(35) Case, D. A.; Darden, T. A.; Cheatham III, T. E.; Simmerling, C. L.; Wang, J.; Duke, R. E.; Luo, R.; Walker, R. C.; Zhang, W.; Merz, K. M.; et al. *AMBER 12*; University of California: San Francisco, 2012.

(36) *CPMD*; Copyright IBM Corp 1990−2008, Copyright MPI fur Festkorperforschung Stuttgart 1997−2001.

(37) Laio, A.; VandeVondele, J.; Rothlisberger, U. A Hamiltonian Electrostatic Coupling Scheme for Hybrid Car-Parrinello Molecular Dynamics Simulations. *J. Chem. Phys.* **2002**, *116*, 6941−6947.

(38) Perdew, J. P.; Burke, K.; Ernzerhof, M. Generalized Gradient Approximation Made Simple. *Phys. Rev. Lett.* **1996**, *77*, 3865−3868.

(39) Kulhánek, P.; Fuxreiter, M.; Štěpán, J.; Koča, J.; Mones, L.; Střelcová, Z.; Petřek, M. *PMFLib - A Toolkit for Free Energy Calculations*; Masaryk University: Brno, Czeck Republic, 2013.

(40) Cremer, D.; Pople, J. General Definition of Ring Puckering Coordinates. *J. Am. Chem. Soc.* **1975**, *97*, 1354−1358.